Implementation and validation of a constitutive model for the cyclic behaviour of interface elements

D.V. Oliveira*, P.B. Lourenço

Department of Civil Engineering, University of Minho, Azurém, 4800-058 Guimarães, Portugal

Abstract

A constitutive model developed for the simulation of the cyclic behaviour of interface elements is proposed. Its theoretical framework is fully based on the plasticity theory. Starting from an existing monotonic model, two new yield surfaces are introduced in order to include non-linear unloading/reloading behaviour in an accurate fashion. The motion of the unloading surfaces is controlled by a mixed hardening law and, by adopting appropriate evolution rules, it is possible to reproduce non-linear behaviour during unloading. Numerical results concerning the analysis of both uniaxial tests and masonry walls are presented and discussed as application and validation examples of the constitutive model.

Keywords: Interface elements; Cyclic behaviour; Plasticity theory; Masonry structures

1. Introduction

Interface elements were initially employed in concrete by Ngo and Scordelis [1], in rock mechanics by Goodman et al. [2] and in masonry by Page [3], being used since then in a great variety of structural problems. The application of a micro-modelling strategy to the analysis of in-plane masonry structures using the finite element method requires the use of continuum elements and line interface elements. Usually, continuum elements are assumed to behave

* Corresponding author. *Tel:* +351 253 510 200; *Fax:* +351 253 510 217; *E-mail:* danvco@civil.uminho.pt

elastically whereas non-linear behaviour is concentrated in the interface elements. This sort of modelling assumes high importance in structures where the interface appears well defined (as in masonry structures) and, therefore, the numerical simulation of the cyclic behaviour of interface elements is definitely a key issue when dealing with micro-modelling. For each type of element referred to above, the respective constitutive model establishes a relation between generalized stress and strain vectors, usually expressed as

$$\boldsymbol{\sigma} = \mathbf{D}\,\boldsymbol{\varepsilon} \tag{1}$$

where $\mathbf{D}$ represents the stiffness matrix. For zero-thickness line interface elements, the constitutive relation defined by Eq. (1) expresses a direct relation between the traction vector and the relative displacement vector along the interface, which read

$$\boldsymbol{\sigma} = \begin{Bmatrix} \sigma \\ \tau \end{Bmatrix}, \quad \boldsymbol{\varepsilon} = \begin{Bmatrix} \Delta u_n \\ \Delta u_t \end{Bmatrix} \tag{2}$$

The development of constitutive models for the analysis of structures submitted to cyclic loading should consider the main relevant features that characterize cyclic behaviour. Recent experimental work [4-7] carried out to investigate cyclic behaviour of interfaces has shown some important characteristics, summarized as

- Stiffness degradation in both tension and compression regimes;
- Residual relative normal displacements at zero stress;
- Absence of stiffness degradation in direct shear;
- Complete crack closing under compressive loading.

Based on the available experimental results concerning the cyclic behaviour of interfaces, the following hypotheses will be assumed in this paper:

- Elastic behaviour constitutes a satisfactory approach for shear unloading/reloading behaviour;

- Elastic unloading/reloading is not an appropriate hypothesis for tensile and compressive loading since observed experimental behaviour cannot be simulated accurately, namely stiffness degradation and crack closing/reopening, which clearly exhibit non-linear behaviour. Accordingly, non-linear constitutive material laws should be adopted.

It becomes clear that the classical formulation of plasticity theory is unable to reproduce these particular features and therefore cannot be used for cyclic loading. However, as shown elsewhere [8-10], this same theory can consistently be extended to incorporate plastic behaviour during unloading. In this work, a rate independent behaviour is considered for the interface constitutive model.

2. Constitutive model

In order to accurately reproduce the main characteristics related to cyclic behaviour of interfaces, a constitutive model is proposed in this paper. For further details, the reader is referred to [11]. This model is fully based on an incremental formulation of plasticity theory and derives from an existing constitutive model developed by Lourenço and Rots [12] for monotonic loading, which includes all the modern concepts used in computational plasticity, such as implicit return mappings and consistent tangent operators.

2.1 Existing constitutive model for monotonic loading

The monotonic constitutive interface model is defined by a convex composite yield criterion, composed by three individual yield functions, where softening behaviour has been included for all modes, reading

$$\begin{aligned} &\text{Tensile criterion:} && f_t(\boldsymbol{\sigma}, \kappa_t) = \sigma - \overline{\sigma}_t(\kappa_t) \\ &\text{Shear criterion:} && f_s(\boldsymbol{\sigma}, \kappa_s) = |\tau| + \sigma \tan\phi - \overline{\sigma}_s(\kappa_s) \\ &\text{Compressive criterion:} && f_c(\boldsymbol{\sigma}, \kappa_c) = \left(\boldsymbol{\sigma}^T \boldsymbol{P} \boldsymbol{\sigma}\right)^{1/2} - \overline{\sigma}_c(\kappa_c) \end{aligned} \tag{3}$$

Here, ϕ represents the friction angle and $\boldsymbol{P}$ is a projection diagonal matrix, based on material parameters. $\overline{\sigma}_t, \overline{\sigma}_s$ and $\overline{\sigma}_c$ are the isotropic effective stresses of each of the adopted yield functions, ruled by the scalar internal variables κ_t, κ_s and κ_c, respectively. In order to obtain a simple relation between the scalar variable κ_c and the plastic multiplier λ_c, the original monotonic compressive criterion, see Eq. $(3)_3$, was rewritten in square root form. The rate expressions for the evolution of the isotropic hardening variables were assumed to be given by

$$\dot{\kappa}_t = \left|\Delta \dot{u}_n\right| = \dot{\lambda}_t \;, \quad \dot{\kappa}_s = \left|\Delta \dot{u}_t\right| = \dot{\lambda}_s \;, \quad \dot{\kappa}_c = \frac{\boldsymbol{\sigma}^T \dot{\boldsymbol{\varepsilon}}^p}{\overline{\sigma}_c} = \dot{\lambda}_c \tag{4}$$

Fig. 1 schematically represents the three individual yield surfaces that compose the multisurface interface model in stress space. Associated flow rules were assumed for tensile and compressive modes and a non-associated plastic potential was adopted for the shear mode, with a dilatancy angle ψ and a cohesion *c*, given by

$$g_s = \left|\tau\right| + \sigma \tan\psi - \overline{\sigma}_s(\kappa_s) \tag{5}$$

A non-associated flow rule for shear is necessary because friction and dilatancy angles are considerably different, as shown by Van der Pluijm [13].

2.2 Constitutive model for cyclic loading

In order to include unloading/reloading behaviour in an accurate manner, an extension of the plasticity theory is presented here. Two new auxiliary yield surfaces (termed unloading surfaces) similar to the monotonic ones were introduced in the monotonic model, so that unloading to tension and to compression could be modelled. Each unloading surface moves inside the admissible stress space towards the similar monotonic yield surface. In a given unloading process, when the stress point reaches the monotonic yield surface, the surface used for unloading becomes inactive and the loading process becomes controlled by the monotonic yield surface. Similarly, if a stress reversal occurs during an unloading process, a new

unloading surface is started, subsequently deactivated when it reaches the monotonic envelope or when a new stress reversal occurs. The proposed model comprises six possibilities for unloading/reloading movements, as schematized in Fig. 2. Two unloading cases from the monotonic envelope are considered: unloading to tension (CT) and unloading to compression (TC). In both cases, a stress reversal can occur even before the monotonic envelope has been reached, leading to reloading movements to compression (CTC) and to tension (TCT), respectively. These two cases may originate two new other movements if a reversal situation happens before stresses reach the monotonic envelope, respectively CTCT and TCTC. If a stress reversal takes place during a CTCT or TCTC movement, reloading movements CTC and TCT are assumed to occur, respectively. The movements to tension (CT, TCT and CTCT) are carried out with the same unloading surface, but different hardening laws, which must be based on reliable experimental data. The same applies to the movements to compression (TC, CTC and TCTC).

Both unloading surfaces are ruled by mixed hardening laws, for which a definition of the back-stress vector $\boldsymbol{\alpha}$ is necessary. In this work, the evolution of the back-stress vector is assumed to be given by [10, 14]

$$\dot{\boldsymbol{\alpha}} = (1-\gamma)\dot{\lambda}_U K_t \boldsymbol{u}_\alpha \tag{6}$$

where K_t is the kinematic tangential hardening modulus, $\dot{\lambda}_U$ is the unloading plastic multiplier rate and $\boldsymbol{u}_\alpha$ is the unitary vector of $\boldsymbol{\alpha}$. Associated flow rules are assumed during unloading to tension and to compression.

Unloading/reloading to tension can be started from any allowable stress point, except from points on the monotonic tensile surface, see Fig. 3(a), ruled according to the yield function

$$f_{Ut}(\boldsymbol{\sigma}, \boldsymbol{\alpha}, \kappa_{Ut}) = \boldsymbol{\xi}^{(1)} - \bar{\sigma}_{i,Ut}(\gamma\kappa_{Ut}) \tag{7}$$

where $\bar{\sigma}_{i,Ut}$ is the isotropic effective stress and κ_{Ut} is the tensile unloading hardening parameter. The scalar γ provides the proportion of isotropic and kinematic hardening ($0 \leq \gamma \leq 1$). The relative (or reduced) stress vector $\boldsymbol{\xi}$ is given by

$$\boldsymbol{\xi} = \boldsymbol{\sigma} - \boldsymbol{\alpha} \tag{8}$$

In the same way, unloading/reloading to compression can take place from any acceptable stress point, except from points on the monotonic compressive surface, see Fig. 3(b), being controlled by the following yield function

$$f_{Uc}(\boldsymbol{\sigma}, \boldsymbol{\alpha}, \kappa_{Uc}) = \left(\boldsymbol{\xi}^T \mathbf{P} \boldsymbol{\xi}\right)^{1/2} - \bar{\sigma}_{i,Uc}(\gamma \kappa_{Uc}) \tag{9}$$

where $\bar{\sigma}_{i,Uc}$ is the isotropic effective stress and κ_{Uc} is the compressive unloading hardening parameter.

The evolution of the hardening parameters is given by

$$\dot{\kappa}_{Ut} = \left|\Delta \dot{u}_n^p\right| = \dot{\lambda}_{Ut} \quad , \quad \dot{\kappa}_{Uc} = \frac{\boldsymbol{\xi}^T \dot{\boldsymbol{\varepsilon}}^p}{\bar{\sigma}_{i,Uc}} = \dot{\lambda}_{Uc} \tag{10}$$

For each of the six hypotheses considered for unloading movements, a curve that relates the unloading hardening parameter κ_U and the unloading effective stress $\bar{\sigma}_U$ must be defined. Thus, the adoption of appropriate evolution rules makes possible to reproduce non-linear behaviour during unloading. Physical reasons imply that C^1 continuity (continuous functions with continuous derivatives) must be imposed on all the six $\bar{\sigma}_U$-κ_U curves. Also, all functions must originate positive effective stress values, their derivatives must always be non-negative and its shape must be adequately chosen to fit experimental data, obtained from uniaxial tests. The six different curves adopted in this study are used in the definition of the isotropic and kinematic hardening laws.

The complete definition of the hardening laws requires the need of four additional material parameters with respect to the monotonic version, which can be obtained from uniaxial cyclic

experiments under tensile and compressive loading. These parameters define ratios between the plastic strain expected at some special points of the uniaxial σ-Δu_n curve and the monotonic plastic strain. Some of these points are schematized in Fig. 4, and are defined as:

- κ_{1t}: plastic strain at zero stress when unloading from the monotonic tensile envelope, see Fig. 4(a);
- κ_{1c}: plastic strain at zero stress when unloading from the monotonic compressive envelope, see Fig. 4(b);
- κ_{2c}: plastic strain at the monotonic tensile envelope when unloading from the monotonic compressive envelope, see Fig. 4(b);
- $\Delta\kappa_c$: plastic strain increment originated by a reloading from a CT or a CTCT unloading movement (stiffness degradation between cycles).

The integration of the non-linear rate equations over the finite step $(\cdot)_n \rightarrow (\cdot)_{n+1}$, by applying an implicit Euler backward integration scheme, allows obtaining the following discrete set of equations [11]:

$$
\begin{aligned}
&\boldsymbol{\sigma}_{n+1} = \mathbf{D}\left(\boldsymbol{\varepsilon}_{n+1} - \boldsymbol{\varepsilon}^{p}_{n+1}\right) \\
&\boldsymbol{\varepsilon}^{p}_{n+1} = \boldsymbol{\varepsilon}^{p}_{n} + \Delta\lambda_{U,n+1}\left.\frac{\partial g_U}{\partial \boldsymbol{\sigma}}\right|_{n+1} \\
&\boldsymbol{\alpha}_{n+1} = \boldsymbol{\alpha}_{n} + (1\text{-}\gamma)\,\Delta\lambda_{U,n+1}\,K_{ks}\,\mathbf{u}_{\alpha,\,n+1} \\
&\kappa_{U,n+1} = \kappa_{U,n} + \Delta\lambda_{U,n+1} \\
&f_{U,n+1}\left(\boldsymbol{\sigma}_{n+1}, \boldsymbol{\alpha}_{n+1}, \kappa_{U,n+1}\right) = 0
\end{aligned}
\tag{11}
$$

where ε^p is the plastic strain and K_{ks} is the kinematic secant hardening modulus, defined as a function of the unloading hardening parameter and the kinematic effective stress [15]. The discrete Kuhn-Tucker conditions at step n+1 are expressed as

$$\lambda_{U,n+1} \geq 0 \;\; , \quad f_{U,n+1}\left(\boldsymbol{\sigma}_{n+1}, \boldsymbol{\alpha}_{n+1}, \kappa_{U,n+1}\right) \leq 0 \;\; , \quad \lambda_{U,n+1}\, f_{U,n+1}\left(\boldsymbol{\sigma}_{n+1}, \boldsymbol{\alpha}_{n+1}, \kappa_{U,n+1}\right) = 0 \qquad (12)$$

Considering an auxiliary elastic trial state, where plastic flow is frozen during the finite step, Eqs. (11) can be reformulated and read

$$\begin{aligned}
&\boldsymbol{\sigma}_{n+1}^{trial} = \boldsymbol{\sigma}_n + \mathbf{D}\Delta\boldsymbol{\varepsilon}_{n+1} \\
&\boldsymbol{\varepsilon}_{n+1}^{p,trial} = \boldsymbol{\varepsilon}_n^{p} \\
&\boldsymbol{\alpha}_{n+1}^{trial} = \boldsymbol{\alpha}_n \\
&\kappa_{U,n+1}^{trial} = \kappa_{U,n} \\
&f_{U,n+1}^{trial} = f_{U,n+1}\left(\boldsymbol{\sigma}_{n+1}^{trial}, \boldsymbol{\alpha}_{n+1}^{trial}, \kappa_{U,n+1}^{trial}\right)
\end{aligned} \qquad (13)$$

A stress reversal occurrence is based on the elastic trial state. After a plastic process (monotonic or cyclic), a stress reversal case is established under the condition of a negative unloading yield function value. Within the notation inserted before, unloading movements CT or TC must be started from the respective monotonic envelope whenever, after a converged load step where $f_n\left(\boldsymbol{\sigma}_n, \kappa_n\right) = 0$, the following condition occurs

$$f_{n+1}^{trial} = f_{n+1}\left(\boldsymbol{\sigma}_{n+1}^{trial}, \kappa_{n+1}^{trial}\right) < 0 \qquad (14)$$

The remaining unloading hypotheses, see Fig. 2, are trigged whenever, after a converged load step in which $f_{U,n}\left(\boldsymbol{\sigma}_n, \boldsymbol{\alpha}_n, \kappa_{U,n}\right) = 0$, the following situation happens

$$f_{U,n+1}^{trial} = f_{U,n+1}\left(\boldsymbol{\sigma}_{n+1}^{trial}, \boldsymbol{\alpha}_{n+1}^{trial}, \kappa_{U,n+1}^{trial}\right) < 0 \qquad (15)$$

The system of non-linear equations expressed by Eqs. (11) can be significantly simplified because the variables $\boldsymbol{\sigma}_{n+1}$, $\boldsymbol{\alpha}_{n+1}$ and $\kappa_{U,n+1}$ can be expressed as functions of $\Delta\lambda_{U,n+1}$ and, therefore, Eq. $(11)_5$ is transformed into a non-linear equation of one single variable. The plastic corrector step consists of computing an admissible value of $\Delta\lambda_{U,n+1}$ that satisfies Eqs. (12), using the Newton-Rapshon method. The necessary derivative reads

$$\left.\frac{\partial f_U}{\partial \Delta\lambda_U}\right|_{n+1} = -\left(\frac{\partial f_U}{\partial \boldsymbol{\sigma}}\right)^T \mathbf{H} \frac{\partial g_U}{\partial \boldsymbol{\sigma}} - h_U \tag{16}$$

where

$$\begin{aligned} \mathbf{H} &= \left[\mathbf{D}^{-1} + \Delta\lambda_{U,n+1} \frac{\partial^2 g_U}{\partial \boldsymbol{\sigma}^2}\right]^{-1} \\ h_U &= (1-\gamma) K_t \left(\frac{\partial f_U}{\partial \boldsymbol{\sigma}}\right)^T \boldsymbol{u}_{\alpha,n+1} - \left.\frac{\partial f_U}{\partial \boldsymbol{\kappa}_U}\right|_{n+1} \end{aligned} \tag{17}$$

Fig. 3 illustrates also that a composite yield criterion, composed by an unloading/shear corner, may occur. These two modes are assumed to be uncoupled, resulting in $\dot{\boldsymbol{\kappa}}_U = \dot{\lambda}_U$ and $\dot{\boldsymbol{\kappa}}_s = \dot{\lambda}_s$. Since all unknowns of the stress vector can be expressed as functions of $\Delta\lambda_{U,n+1}$ and $\Delta\lambda_{s,n+1}$, the system of non-linear equations to be solved can be reduced to

$$\begin{cases} f_s\left(\Delta\lambda_{U,n+1}, \Delta\lambda_{s,n+1}\right) = 0 \\ f_U\left(\Delta\lambda_{U,n+1}, \Delta\lambda_{s,n+1}\right) = 0 \end{cases} \tag{18}$$

The components of the Jacobian necessary for the iterative Newton-Raphson procedure to solve this system can be found in [11].

Each time a stress reversal takes place, a new unloading surface is activated, being deactivated when it reaches the monotonic envelope towards which it moves, thus, for the same load step, yielding may occur both on the unloading surface and on the monotonic surface. Therefore, a sub-incremental procedure must be used in order to split such load increment into two sub-increments, each one corresponding to a different yield surface. In a strain driven process, in which the total strain vector is the only independent variable, the problem consists in the computation of the scalar $0 < \beta < 1$

$$\boldsymbol{\varepsilon}_{n+1} = \boldsymbol{\varepsilon}_n + \beta \Delta\boldsymbol{\varepsilon}_{n+1} + (1-\beta)\Delta\boldsymbol{\varepsilon}_{n+1} \tag{5.1}$$

for which the strain increment $\beta\Delta\boldsymbol{\varepsilon}_{n+1}$ leads the unloading surface to touch the monotonic one. After the deactivation of the unloading surface, the remaining strain increment $(1\text{-}\beta)\Delta\boldsymbol{\varepsilon}_{n+1}$ is used for the monotonic surface. In the present implementation, β is computed through the bisection method, where the monotonic yield function is evaluated at each iteration.

2.3 Performance of the model under uniaxial loading

The ability of the proposed constitutive model to simulate experimental results is now assessed by comparisons with reputed available experimental data obtained under uniaxial loading conditions. The results were graphically scaled on peak experimental displacement and stress values, for a better comparison.

A direct shear test on mortar joints carried out by Atkinson et al. [4] is used here to evaluate the ability of the model to predict cyclic shear loading assuming elastic unloading/reloading behaviour. The comparison between the experimental data and the numerical response is shown in Fig. 5. A good agreement can be found between the experimental and the numerical results. As assumed in the proposed formulation, elastic behaviour for shear unloading/reloading showed to be a good approximation of the experiments. The hypothesis of exponential softening also seemed to be appropriate for shear monotonic loading.

The ability of the model to capture the main features related to cyclic tensile behaviour is now checked against the experimental results of Gopalaratnam and Shah [16] on concrete specimens. The comparison between experimental and numerical results is shown in Fig. 6. The experimental data was modified in order to express a σ-Δu relationship. The numerical response is in good agreement with the experimental results, namely in terms of stiffness degradation. However, a better agreement could be found if monotonic exponential softening was replaced by a more suitable law [17].

The experiments carried out by Karsan and Jirsa [18] on concrete specimens under cyclic compressive loading are used here to appraise the ability of the model to simulate cyclic compressive loading. The experimental and numerical results are compared in Fig. 7. The experimental results were modified in order to express a σ-Δu relationship. Characteristic features such as stiffness degradation during each unloading/reloading cycle and between cycles are simulated by the model in an appropriate fashion.

The last uniaxial example presented here deals with a tensile-compressive loading test performed by Reinhardt [19] on a concrete specimen. Only six loading cycles were simulated. The comparison between experimental and numerical results is shown in Fig. 8. In spite of the complex cyclic behaviour exhibited by the experimental result, namely stiffness changes associated with the closing and reopening of cracks, the model showed to be able to accurately describe the experimental behaviour.

3. Numerical examples

The ability of the model to reproduce the main features that characterize cyclic behaviour as well as to reproduce experimental results in structural elements is now assessed through the numerical analysis of three masonry walls submitted to cyclic loads. In these simulations, the units were modelled using eight-node continuum plane stress elements with Gauss integration and, for the joints, six-node zero-thickness line interface elements with Lobatto integration were used. All material parameters are discussed in [11].

3.1 TUE wall

Within the scope of the CUR project, Raijmakers and Vermeltfoort [20-21] tested several masonry shear walls submitted to monotonic loads. The walls were made of wire-cut solid clay bricks with dimensions of 210×52×10 mm^3 and 10 mm thick mortar joints and characterized by a height/width ratio of one, with dimensions of 1000×990 mm^2. The shear

walls were built with eighteen courses, from which only sixteen were considered active, since the two extreme courses were clamped in steel beams.

During testing, different vertical uniform loads were initially applied to the walls. Then, for each level of vertical load, a horizontal displacement was imposed at the top steel beam, keeping the top and bottom steel beams horizontal and preventing any vertical movement of the top steel beam. For the purpose of investigating cyclic behaviour, a wall submitted to an average compressive stress value of 1.21 N/mm^2 is considered here. In what follows, the wall to be numerically tested is denoted as TUE wall. Since the wall was tested under monotonic loading, the main purpose of this numerical analysis is to assess the qualitative ability of the model to simulate features related to cyclic behaviour, such as stiffness degradation and energy dissipation.

In order to investigate the cyclic behaviour of the TUE wall, it was decided to submit it to a set of loading-unloading cycles by imposing increasing horizontal displacements at the top steel beam, where unloading was performed at +1.0 mm, +2.0 mm, +3.0 mm and +4.0 mm, until a zero horizontal force value was achieved. The numerical horizontal load-displacement diagram, obtained using the proposed model and following the described procedure, is shown in Fig. 9, where the evolution of the total energy is also given. Fig. 9(a) shows that the cyclic horizontal load-displacement diagram follows closely the monotonic one aside from the final branch, where failure occurs for a smaller horizontal displacement. Unloading is performed in a quite linear fashion showing important stiffness degradation between cycles, while reloading presents initially high stiffness due to closing of diagonal cracks and then is followed by a progressive decrease of stiffness (reopening). In this way, the sequence of the unloading-reloading cycles originates a structural response characterized by a light strength degradation (around 4%) as well as noticeable stiffness degradation. From Fig. 9 it can also be observed that the energy dissipated in an unloading-reloading cycle is increased from cycle to

cycle. In [11], the same wall is analysed under load reversal, for which a 13% strength degradation was reached, see Fig. 10. It was found that the geometric asymmetry in the micro-structure (units) influenced significantly the structural behaviour of the wall. It is also clear from these analyses that masonry shear walls with diagonal zigzag cracks possess an appropriate seismic behaviour with respect to energy dissipation.

Fig. 11 illustrates the incremental deformed meshes with the principal compressive stresses depicted on them, for imposed horizontal displacements corresponding to +4 mm and to a zero horizontal force after unloading from +4.0 mm. Initially, the structural response is characterized by the formation of a single, large, compressive strut. During unloading to zero force, cracked head joints are partially closed and bed joints slide in the opposite direction. The evolution of the diagonal cracks clearly leads to the development of two struts, one at each side of the diagonal line. The softening behaviour that appears after peak load is caused by compressive crushing of the lower toe of the wall, which eventually leads to failure.

3.2 JRC walls

Within the framework of a research program on the assessment of the seismic vulnerability of existing masonry buildings, two masonry walls were tested at the Joint Research Centre (JRC), Italy [22]. Henceforth, these walls are here referred to as JRC walls.

The two walls were made of 250×120×55 mm^3 brick units and hydraulic lime mortar, arranged in two-wythes thickness English bond pattern with the same width of 1000 mm, the same thickness of 250 mm, the same joint thickness of 10 mm, but different heights. The higher wall presents a height/width ratio of 2.0 whereas the lower wall presents a ratio of 1.35. The experimental results showed that the different height/width ratio implies important changes in the wall's overall behaviour. These changes are most certainly related to the activation of different mechanisms of non-linearity, namely cracking of the joints, frictional

sliding along the joints, tensile and shear rupture of the units and compressive failure of masonry.

Experimental load and boundary conditions were chosen in order to reproduce the real conditions experienced by the walls during a seismic occurrence as well as possible. In this way, a vertical uniform compressive load was initially applied. Then, a quasi-static cyclic horizontal displacement was imposed on the steel beam, at the top of the walls. The experimental set-up was such that the steel beam was prevented from rotating, thus allowing the same vertical and horizontal displacements at all points of the beam. Both walls were initially subjected to an average normal stress of 0.6 N/mm^2. Keeping this vertical load constant, alternated increasing in-plane horizontal displacements were imposed on the walls using a cyclic and increasing procedure.

Fig. 12 presents numerical and experimental results in terms of the horizontal load-displacement diagram at the top of the high wall. Moreover, for a better understanding of the cyclic behaviour of the wall, Fig. 13 represents the principal compressive stresses represented on the incremental deformed meshes, for lateral displacements of +12.5 mm and -12.5 mm.

The numerical response clearly indicates that the high wall submitted to alternate horizontal displacements simply rocks in both ways. The highly non-linear shape of the load-displacement curve is essentially due to the opening and subsequent closing, under load reversal, of the top and bottom bed joints, which is evidenced by Fig. 13. Similar deformed patterns, involving the opening of extreme bed joints, were observed during the experimental test [22]. Numerical results show that the cyclic behaviour of the wall is controlled by the opening and closing of the extreme bed joints, where damage is mainly concentrated. The model also shows low energy dissipation, which is a consequence of the activated non-linear mechanism (opening-closing of joints). The comparison between experimental and numerical results shows that the constitutive model is able to accurately reproduce the experimental

cyclic response of the high wall, in terms of maximum load (F_{exp}=72 kN and F_{num}=67.6 kN), global load-displacement diagram, hystereses cycles and total energy evolution as well as in terms of deformed mesh.

Such satisfactory results were not possible to achieve for the low wall. Numerical failure started earlier than in the experiment, although the obtained failure mode was similar to the experimental one. Fig. 14 illustrates the numerical and experimental horizontal load-displacement diagrams at the top of the wall. Before numerical failure was attained, numerical and experimental responses were fairly similar, aside from the peak load, which is higher for the numerical result. Fig. 15 represents the principal compressive stresses depicted on the incremental deformed meshes, for lateral displacements of +4.5 mm and -2.9 mm (numerical failure). Unloading and subsequent reloading causes damage in the same area, leading to the formation of a kind of vertical crack, only interrupted by the units, which were not allowed to crack. This kind of alignment of vertical cracks is the main cause leading to initiation of failure. These deformed patterns were also observed during the experimental testing.

A few reasons can be associated to the premature numerical failure of the wall. A first reason can be related to model parameters. The choice of the parameter values was based on average experimental values, when available, and on estimated values, motivated by the lack of appropriate experimental data. Possibly, the numerical response can be sensitive to a given parameter, not correctly estimated. For instance, the overestimation of the peak load could probably be surpassed if a lower value of the compressive strength was adopted. But this objective was not pursued here. Another reason might be related to the adopted modeling strategy. Potential vertical cracks in the middle of the units were not included in the model since their consideration usually leads to sudden load falls in the load-displacement diagram, associated with numerical cracking in the middle of the unit. As a result, their inclusion generally affects the robustness of the numerical model.

4. Conclusion

A new constitutive model entirely founded on the incremental theory of plasticity and able to describe the cyclic loading of interface elements is presented in this paper. New yield surfaces were introduced in an existing monotonic model, where each unloading surface can only move inside the admissible stress space and towards the similar monotonic yield surface. Their motion is controlled by a mixed hardening law. In this way, the normal stress component is described in a non-linear fashion whereas elastic unloading is assumed only for the shear component.

The comparison between uniaxial experimental and numerical results shows that the most relevant characteristics observed in experiments are captured by the model. These results clearly show the need to consider non-linear material behaviour for the normal stress component during unloading.

The performance of the developed constitutive model was investigated against three masonry walls. The numerical results have shown that the model is able to reproduce the main features that characterize cyclic behaviour, namely stiffness degradation, energy dissipation and deformed patterns, which enables its use for the analysis of masonry structures under cyclic loading. Important differences concerning the structural behaviour, failure mode and dissipated energy were found between the three shear-walls studied.

5. Acknowledgements

The financial support provided by the Portuguese Science and Technology Foundation (PRAXIS XXI BD/16168/98 grant) is gratefully acknowledged.

6. References

[1] Ngo D, Scordelis AC. Finite element analysis of reinforced concrete beams. J. Amer. Concr. Inst. 1967; 64(3): 152-163.

[2] Goodman RE, Taylor, RL, Brekke TL. A model for the mechanics of jointed rock. J. Soil Mech. Found. Div. ASCE 1968; 94(3): 637-659.

[3] Page AW. Finite element model for masonry. J. Struct. Div. ASCE 1978; 104(8): 1267-1285.

[4] Atkinson RH, Amadei BP, Saeb S, Sture S. Response of masonry bed joints in direct shear. J. Struct. Eng. ASCE 1989; 115(9): 2276-2296.

[5] Stankowski T, Runesson K, Sture S. Fracture and slip of interfaces in cementitious composites. I: characteristics. J. Eng. Mech. ASCE 1993; 119(2): 292-314.

[6] Jefferson AD, Mills NR. Fracture and shear properties of concrete construction joints from core samples. Materials and Structures 1998; 31: 595-601.

[7] Lourenço, PB, Ramos LF. Characterization of the cyclic behavior of dry masonry joints. J. Struct. Eng. ASCE 2004; May (accepted for publication).

[8] Pan Y-W. Generalized nonassociative multisurface approach for granular materials. J. Geotech. Eng. ASCE 1991; 117(5): 1336-1353.

[9] Combescure D, Pegon P. A plasticity-based masonry model reproducing the compressive strength degradation under cyclic loading. Special Publication Nº I.96.70, JRC, Ispra, Italy, 1996.

[10] Cachim PB, Figueiras JA, Pereira PA. Numerical modelling of fibre-reinforced concrete fatigue in bending. Int. J. Fatigue 2002; 24: 381-387.

[11] Oliveira DV. Experimental and numerical analysis of blocky masonry structures under cyclic loading. PhD. Dissertation, Universidade do Minho, Guimarães, Portugal, 2003. (also available at www.civil.uminho.pt/masonry)

[12] Lourenço PB, Rots JG. A multi-surface interface model for the analysis of masonry structures. J. Eng. Mech. ASCE 1997; 123(7): 660-668.

[13] Van der Pluijm R. Shear behaviour of bed joints. In: Hamid AA, Harris HG, editors. Proc. 6th North American Masonry Conference 1993; 1: 125-136.

[14] Feenstra PH. Computational aspects of biaxial stress in plain and reinforced concrete. PhD. Dissertation, Delft University of Technology, Delft, The Netherlands, 1993.

[15] Feenstra P, De Borst R. The Rankine plasticity model for concrete cracking. Computational Plasticity. Fundamentals and Applications, Barcelona, 1992: 657-668.

[16] Gopalaratnam VS, Shah SP. Softening response of plain concrete in direct tension. ACI Journal 1985; 82: 310-323.

[17] Hordijk DA. Local approach to fatigue of concrete. Ph.D. Dissertation, Delft University of Technology, Delft, The Netherlands, 1991.

[18] Karsan ID, Jirsa O. Behaviour of concrete under compressive loadings. J. Struct. Div. ASCE 1969; 95: 2543-2563.

[19] Reinhardt HW. Fracture mechanics of an elastic softening material like concrete. Heron 1984; 29(2):3-41.

[20] Raijmakers TMJ, Vermeltfoort AT. Deformation controlled tests in masonry shear walls (in Dutch). Report B-92-1156, TNO-Bow, Delft, The Netherlands, 1992.

[21] Vermeltfoort AT, Raijmakers TMJ. Deformation controlled tests in masonry shear walls, part 2 (in Dutch). Report TUE/BKO/93.08, Eindhoven University of Technology, Eindhoven, The Netherlands, 1993.

[22] Anthoine A, Magonette G, Magenes G. Shear-compression testing and analysis of brick masonry walls. In: Duma G, editor. Proc. 10th European Conference on Earthquake Engineering 1995; 3: 1657-1662.

FIGURE CAPTIONS

Fig. 1 Existing multisurface interface model (stress space) [12].

Fig. 2 Adopted hypotheses for cyclic behaviour (E stands for elastic, C for compression and T for tension).

Fig. 3 Hypothetic motion of the unloading surface in stress space to: (a) tension and to (b) compression.

Fig. 4 Special points at the uniaxial σ-Δu curve: (a) tensile loading and (b) compressive loading.

Fig. 5 Direct shear test under cyclic loading (scaled σ-Δu curve).

Fig. 6 Uniaxial tensile test under cyclic loading (scaled σ-Δu curve).

Fig. 7 Uniaxial compressive test under cyclic loading (scaled σ-Δu curve).

Fig. 8. Cyclic tensile-compressive loading test (scaled σ-Δu curve).

Fig. 9 TUE wall: (a) Horizontal load-displacement diagram, where the dotted line represents the monotonic curve; (b) total energy evolution.

Fig. 10 TUE wall: horizontal load-displacement diagram under load reversal (the dashed lines represent the maximum monotonic loads).

Fig. 11 TUE wall: Principal compressive stresses [N/mm^2] depicted on the incremental deformed mesh for a horizontal displacement corresponding to: (a) +4.0 mm; (b) zero horizontal force after unloading from +4.0 mm.

Fig. 12 Horizontal load-displacement diagram of the high wall: (a) numerical; (b) experimental (from [23]).

Fig. 13 High wall: Principal compressive stresses [N/mm^2] depicted on the incremental deformed mesh for a horizontal displacement equal to: (a) +12.5 mm, (b) -12.5 mm.

Fig. 14 Horizontal load-displacement diagram of the low wall: (a) numerical; (b) experimental (from [23]).

Fig. 15 Low wall: Principal compressive stresses [N/mm^2] depicted on the incremental deformed mesh for a horizontal displacement equal to: (a) +4.5 mm, (b) -2.9 mm.

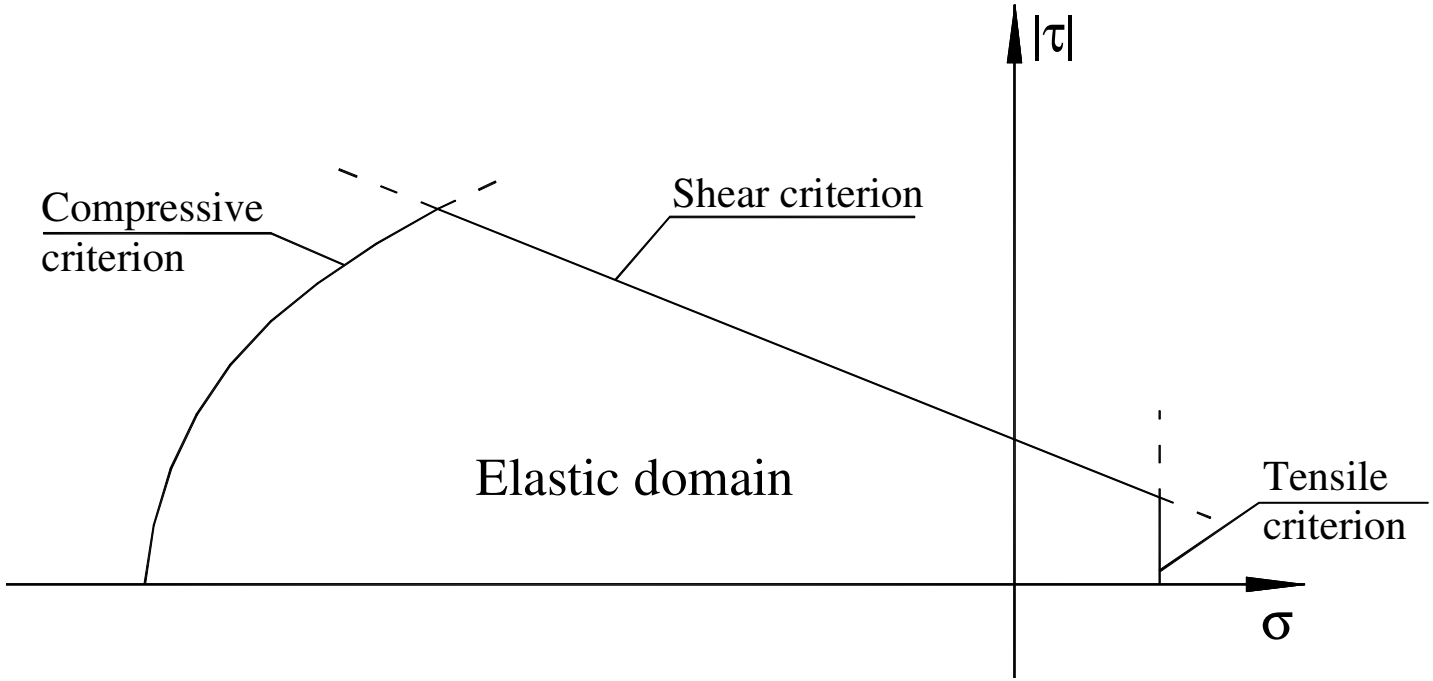

Fig. 1. Existing multisurface interface model (stress space) [12].

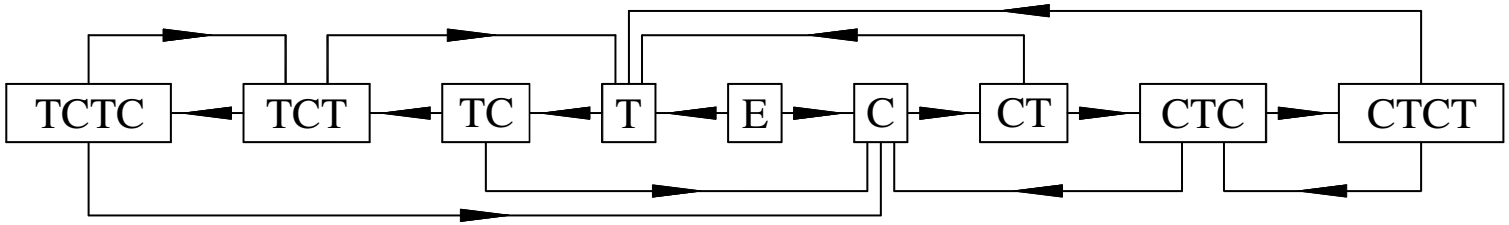

Fig. 2. Adopted hypotheses for cyclic behaviour (E stands for elastic, C for compression and T for tension).

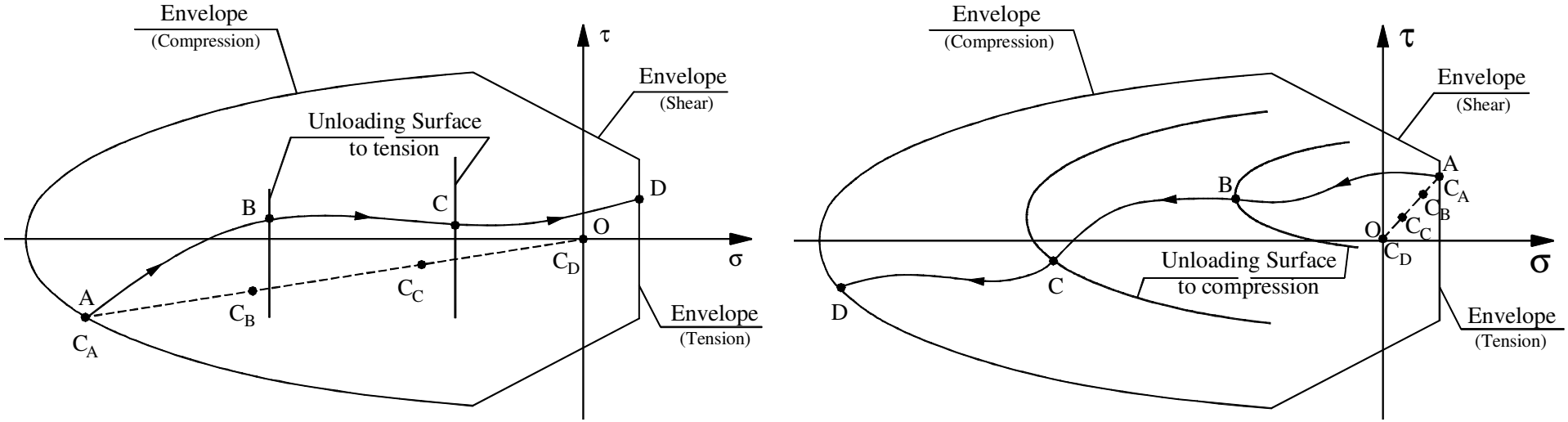

Fig. 3. Hypothetic motion of the unloading surface in stress space to: (a) tension and to (b) compression.

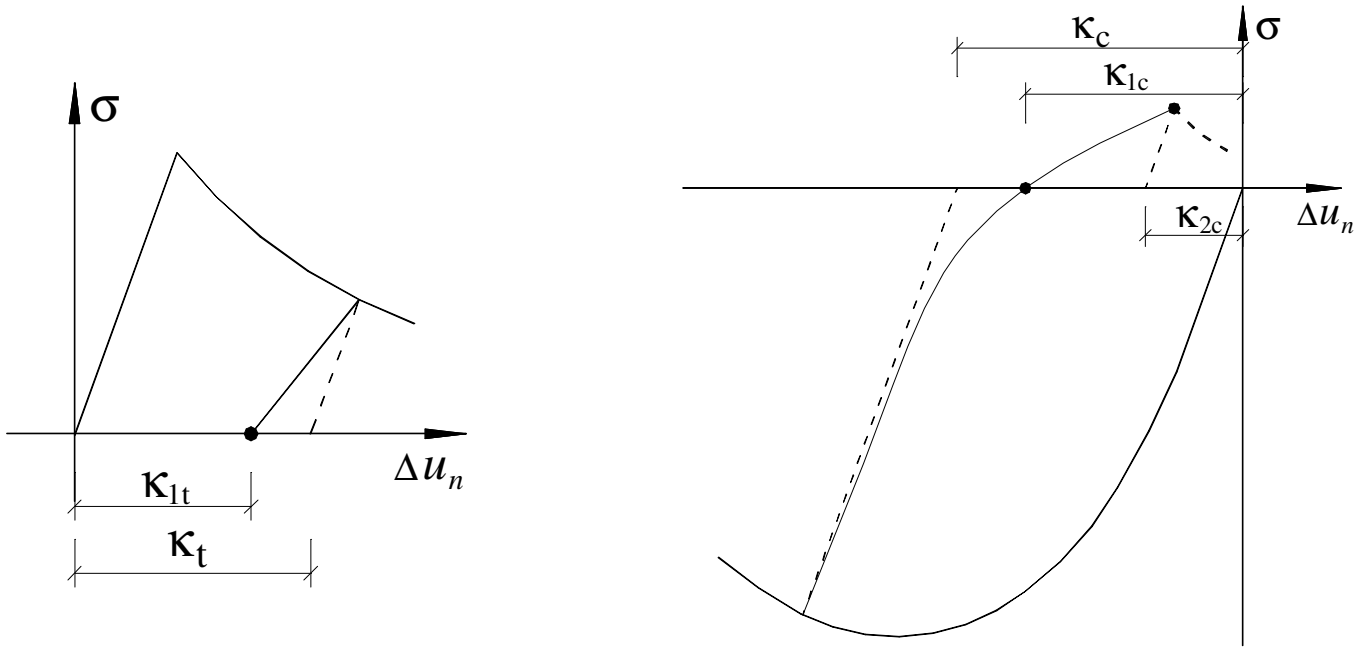

(a) (b)

Fig. 4. Special points at the uniaxial σ-Δu curve: (a) tensile loading and (b) compressive loading.

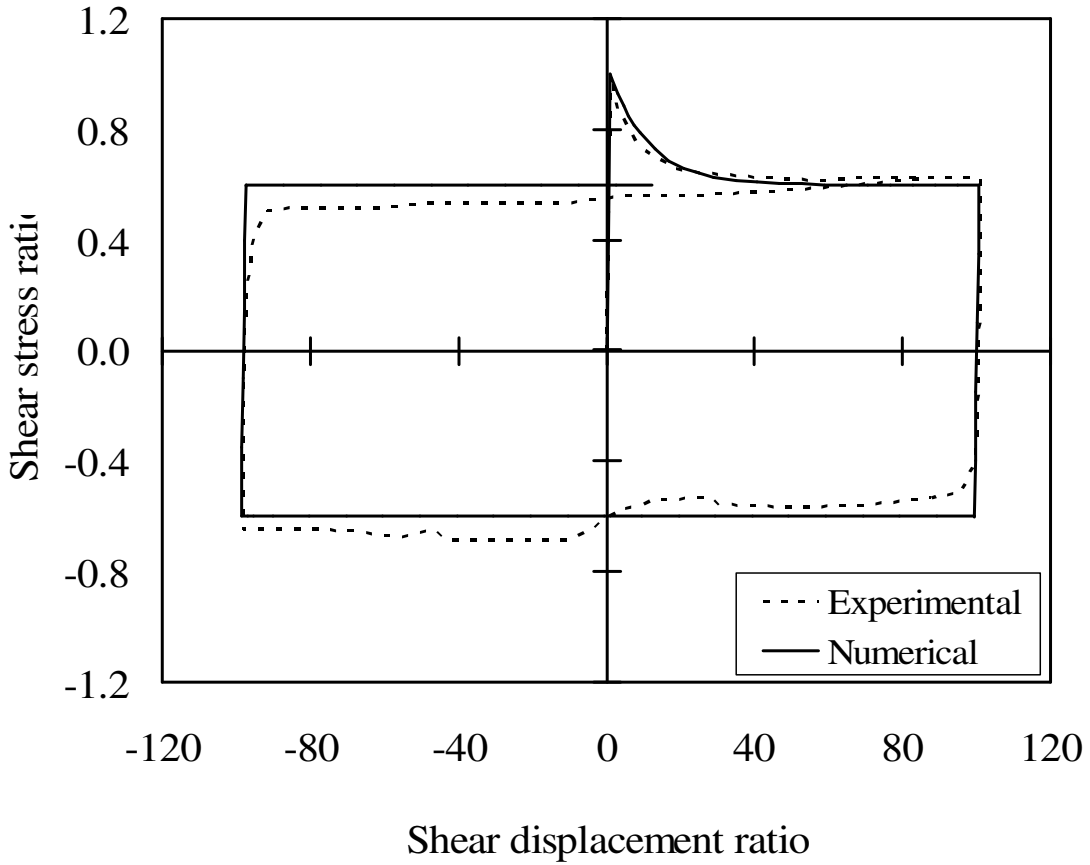

Fig. 5. Direct shear test under cyclic loading (scaled σ-Δu curve).

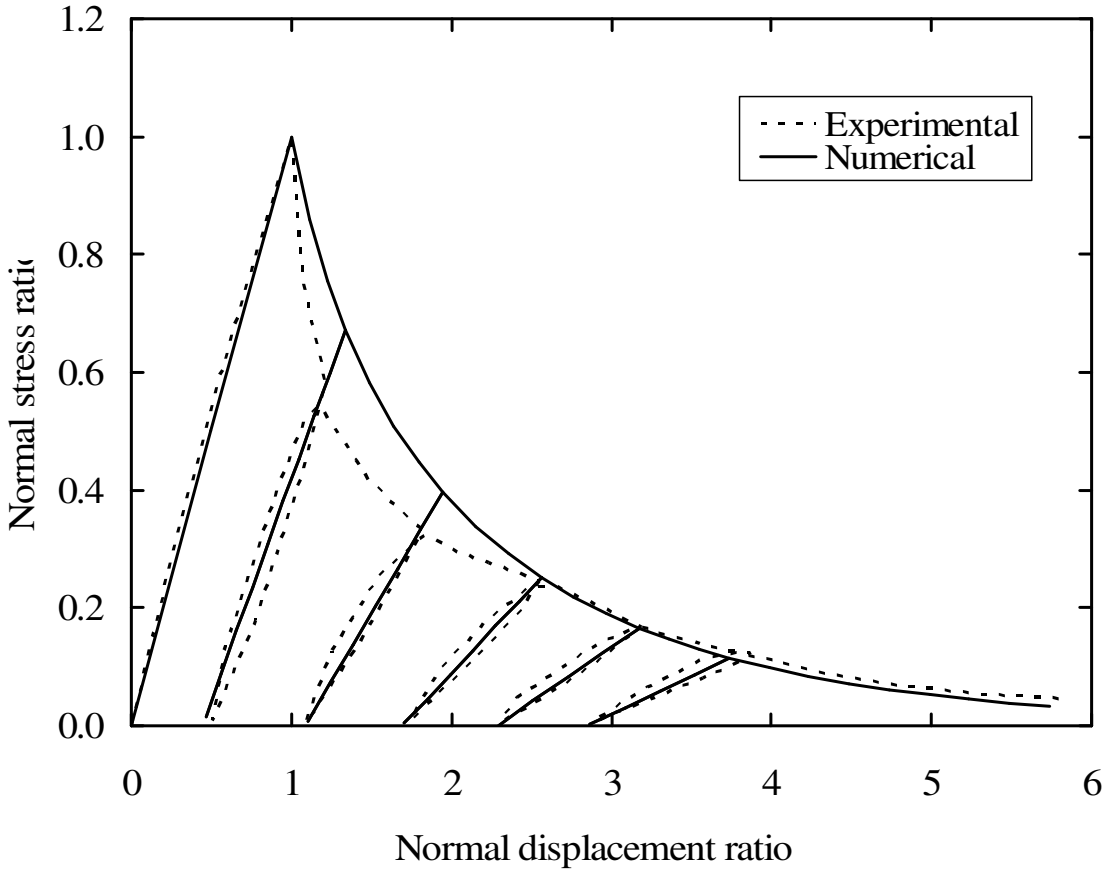

Fig. 6. Uniaxial tensile test under cyclic loading (scaled σ-Δu curve).

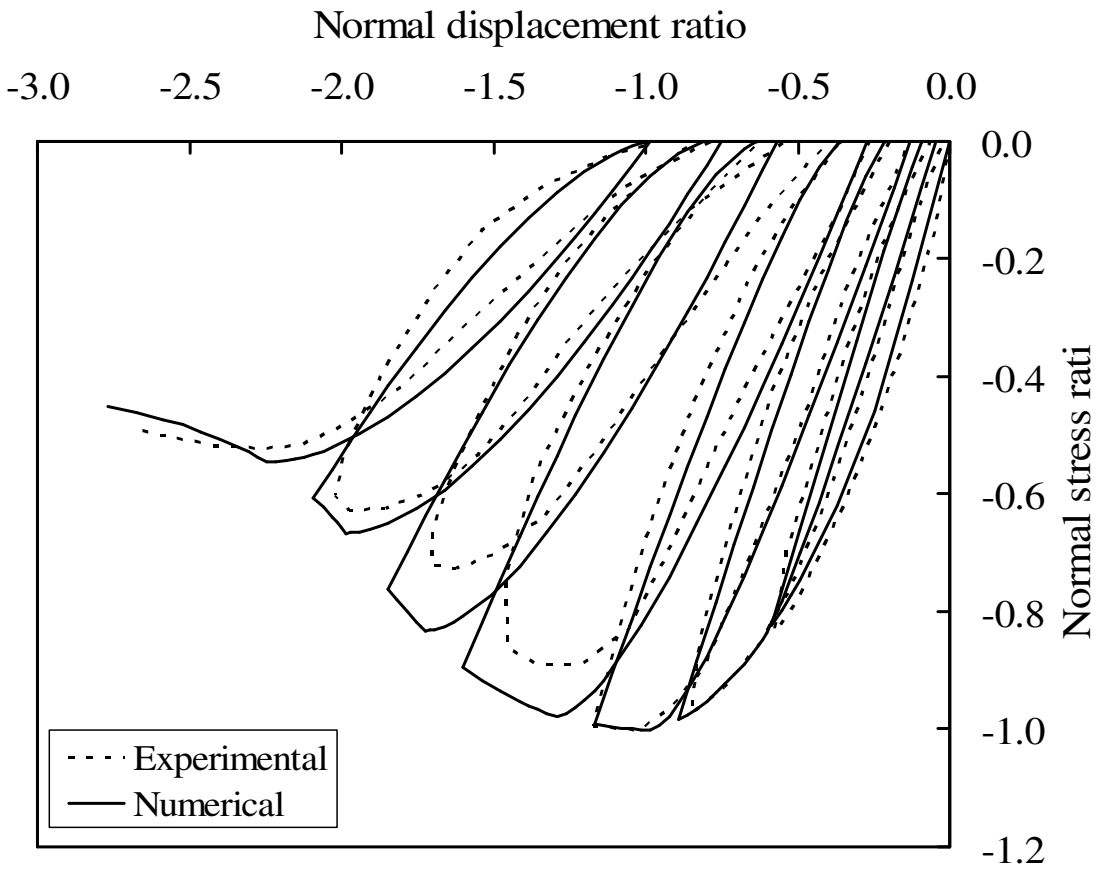

Fig. 7. Uniaxial compressive test under cyclic loading (scaled σ-Δu curve).

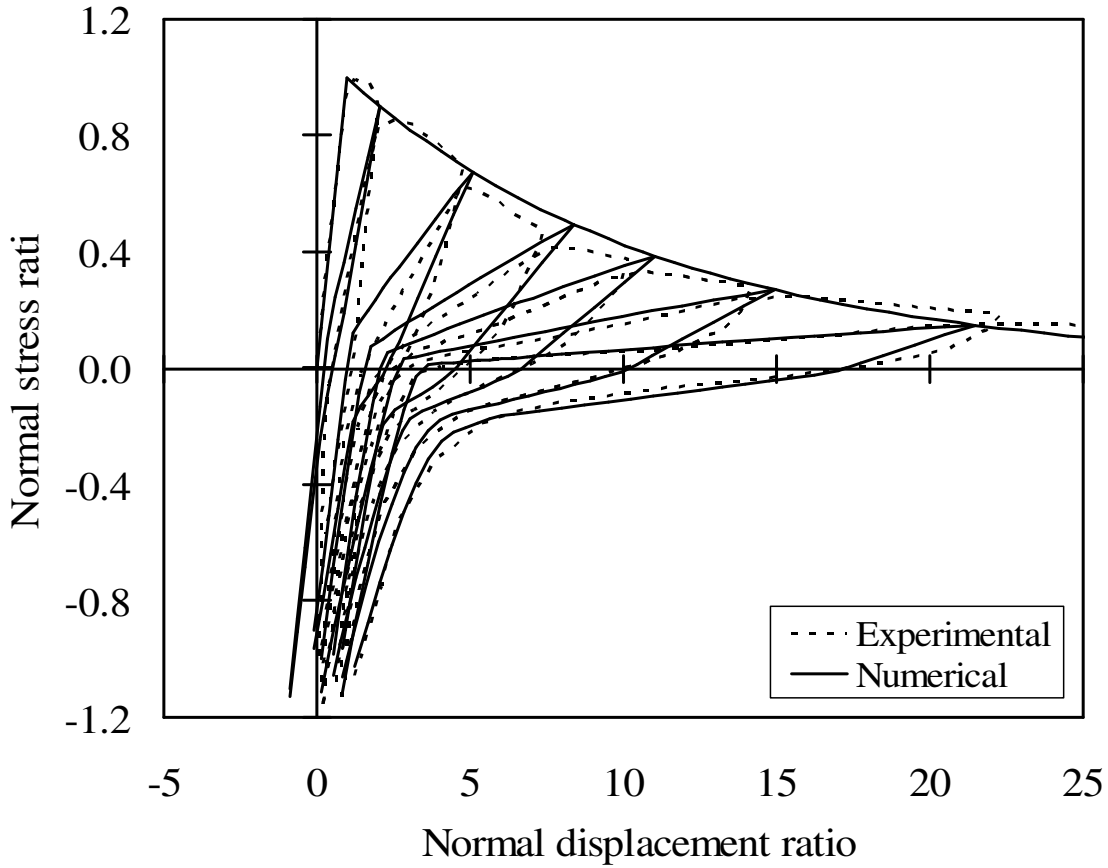

Fig. 8. Cyclic tensile-compressive loading test (scaled σ-Δu curve).

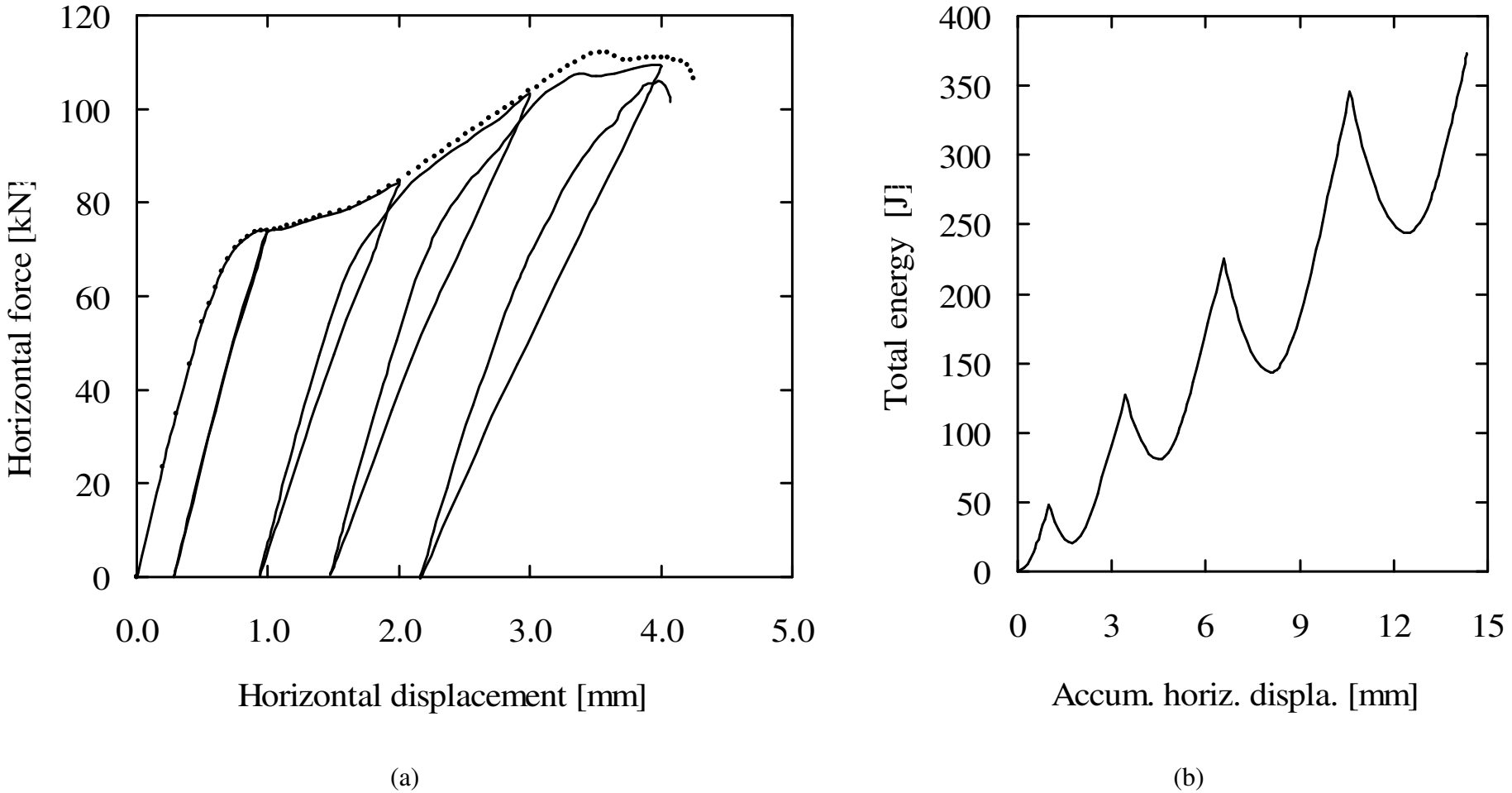

Fig. 9. TUE wall: (a) Horizontal load-displacement diagram, where the dotted line represents the monotonic curve; (b) total energy evolution.

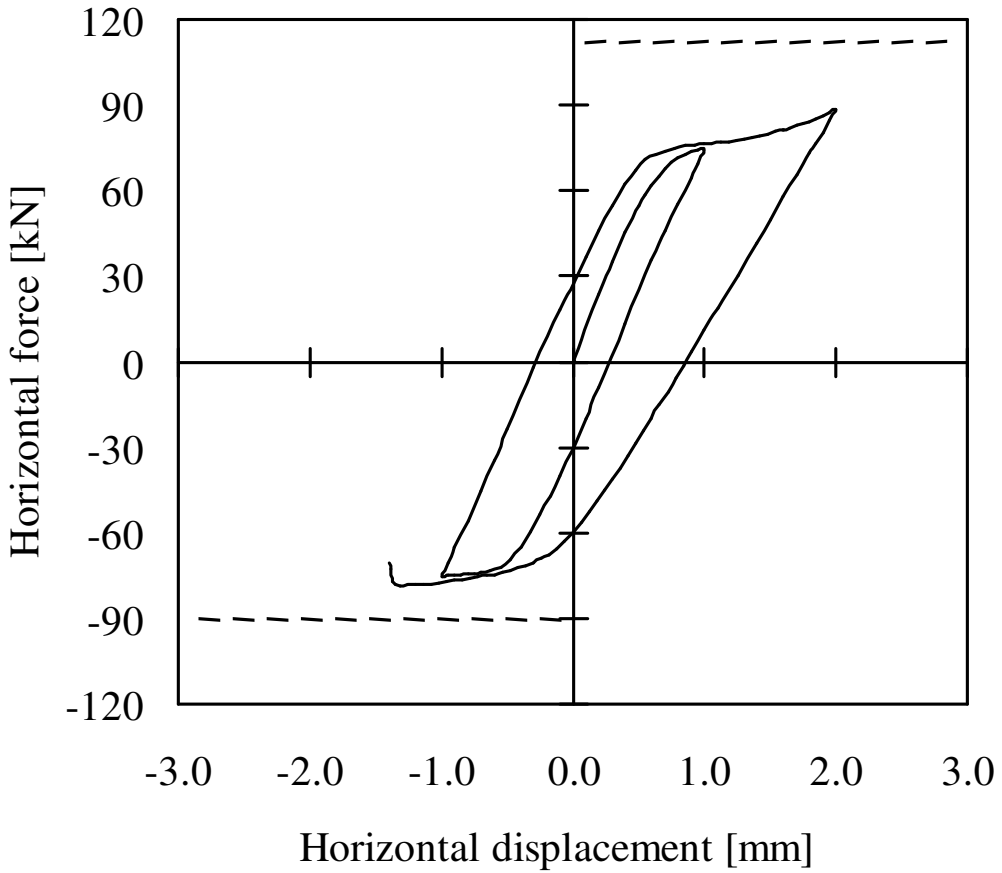

Fig. 10. TUE wall: horizontal load-displacement diagram under load reversal (the dashed lines represent the maximum monotonic loads).

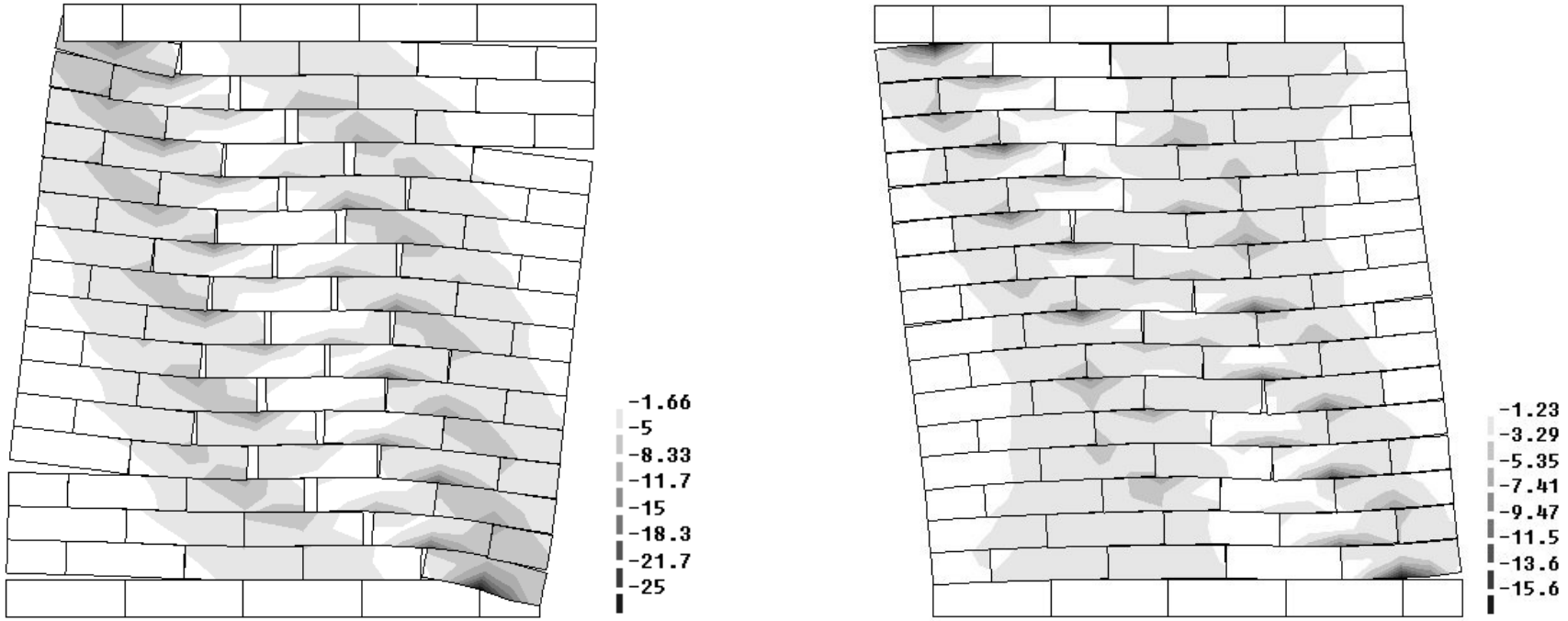

(a) (b)

Fig. 11. TUE wall: Principal compressive stresses [N/mm^2] depicted on the incremental deformed mesh for a horizontal displacement corresponding to: (a) +4.0 mm; (b) zero horizontal force after unloading from +4.0 mm.

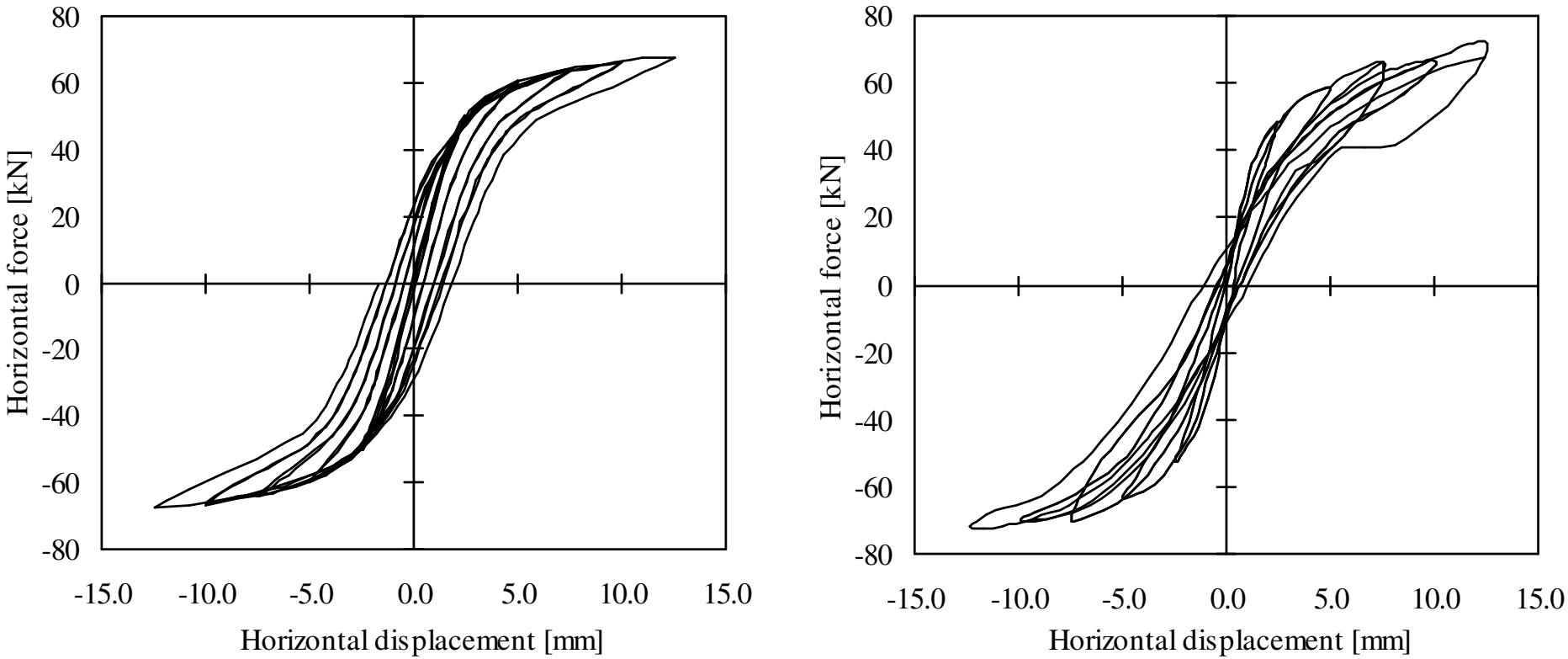

Fig. 12. Horizontal load-displacement diagram of the high wall: (a) numerical; (b) experimental (from [22]).

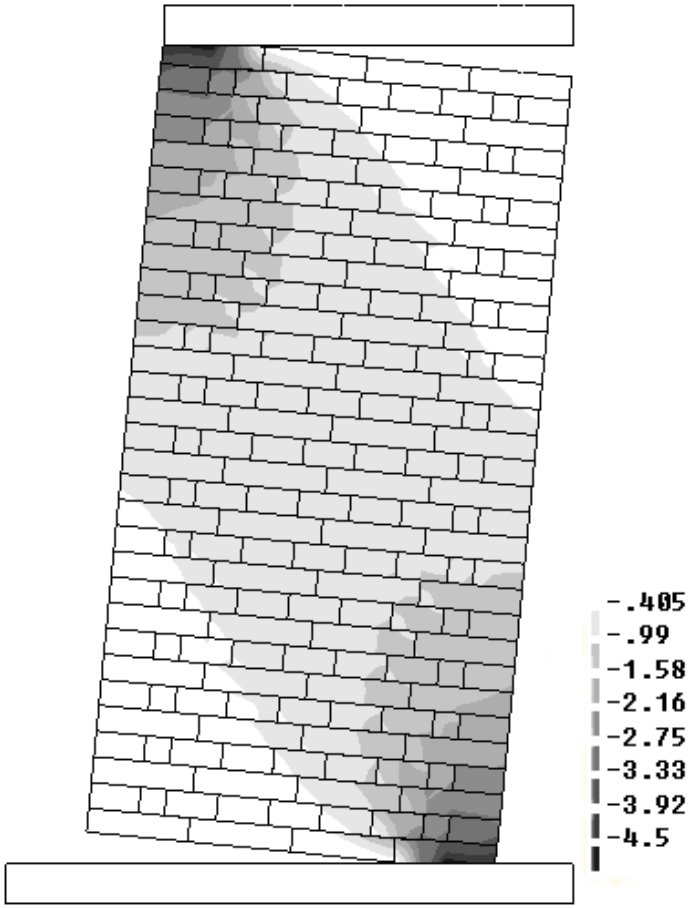

(a)

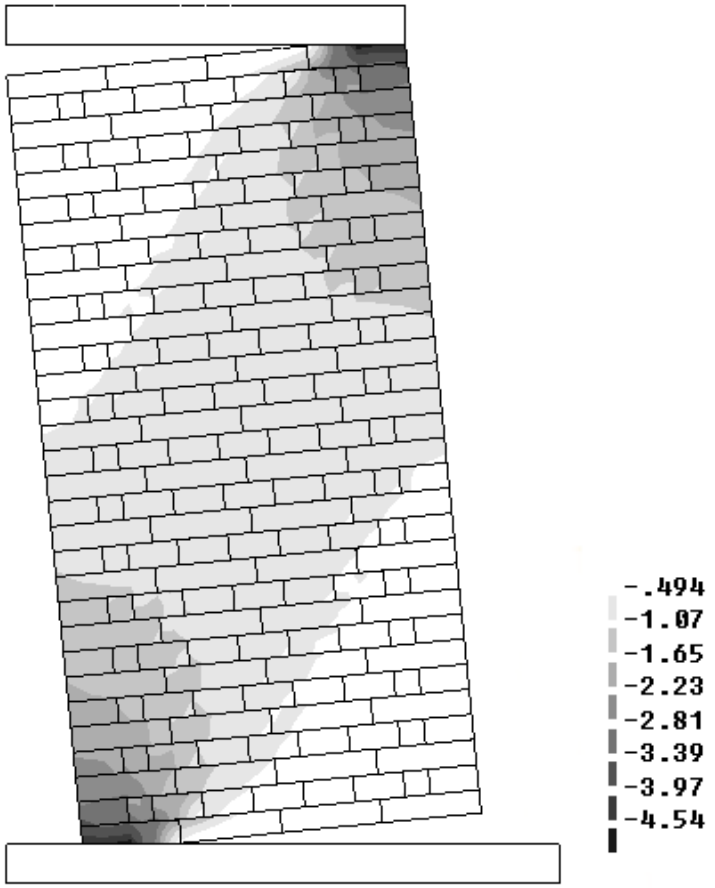

(b)

Fig. 13. High wall: Principal compressive stresses [N/mm^2] depicted on the incremental deformed mesh for a horizontal displacement equal to:

(a) +12.5 mm, (b) -12.5 mm.

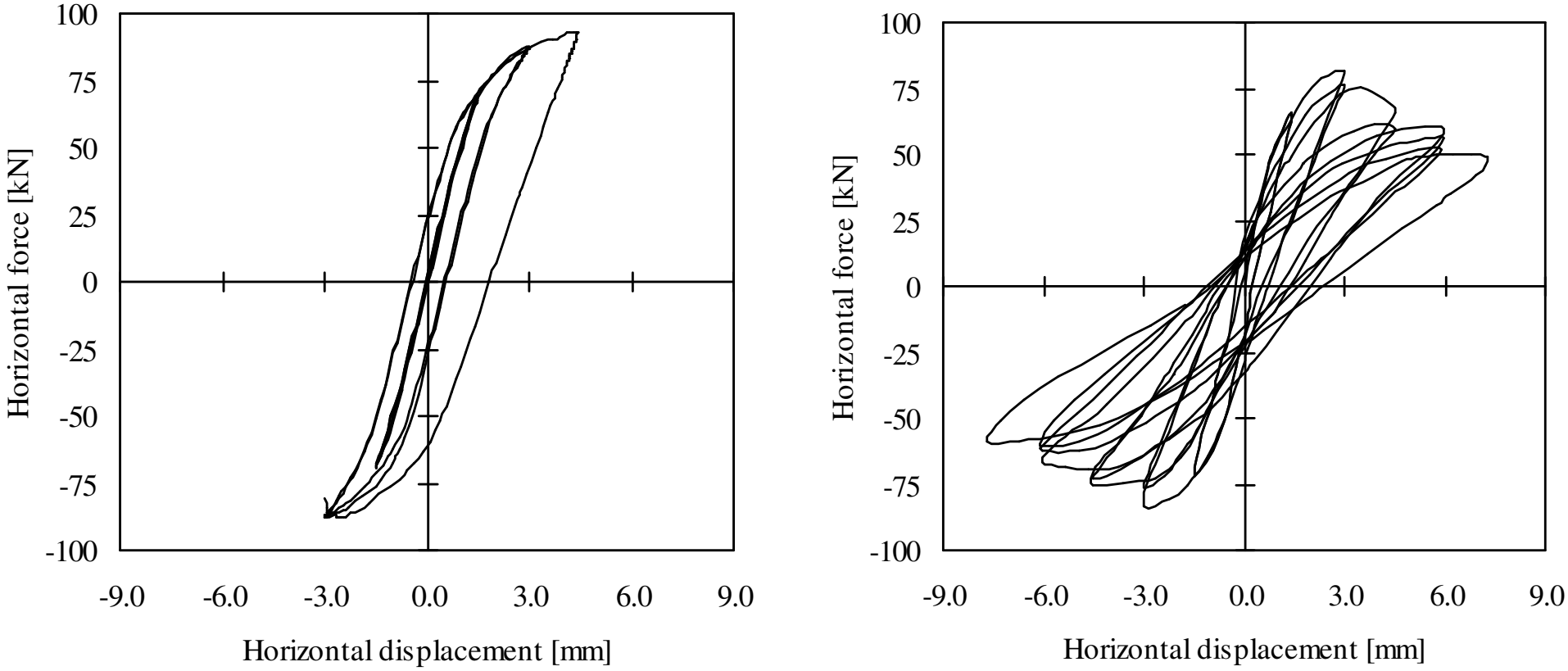

Fig. 14. Horizontal load-displacement diagram of the low wall: (a) numerical; (b) experimental (from [22]).

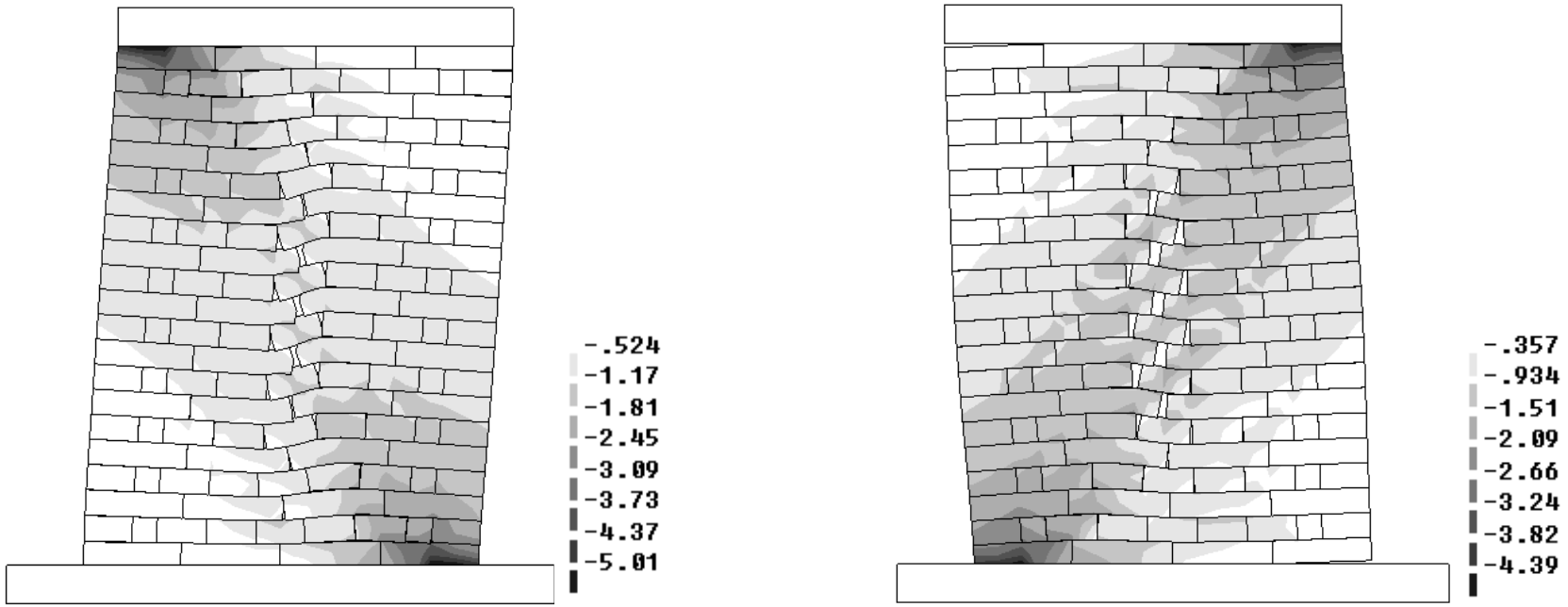

(a) (b)

Fig. 15. Low wall: Principal compressive stresses [N/mm^2] depicted on the incremental deformed mesh for a horizontal displacement equal to:

(a) +4.5 mm, (b) -2.9 mm.